MODELLING COMPLEX ACTUATOR AND SENSOR ARCHITECTURES FOR GUST ALLEVIATION SYSTEMS FOR FLEXIBLE AIRCRAFT

Stefanie Düssler[1], Thulasi Mylvaganam[1], Rafael Palacios[1]

[1]Imperial College London
SW7 2AZ London, United Kingdom
s.dussler20@imperial.ac.uk
t.mylvaganam@imperial.ac.uk
r.palacios@imperial.ac.uk

Keywords: gust load alleviation, LQG, control design

Abstract: We propose a modular framework for designing and testing control systems for flexible air vehicles that may exhibit geometric nonlinearities and rigid/elastic couplings. This framework supports various controllers and levels of modeling fidelity. It can accurately model nonlinear aeroelastic effects and function as a model-in-the-loop using a network interface. We demonstrate its capabilities using an aircraft model with large wing deformations. A linear quadratic Gaussian controller is developed based on a linear reduced-order model derived from the aircraft's cruise flight nonlinear equilibrium and designed for gust alleviation. In the design process, we observe substantial rigid/elastic coupling effects in the aircraft, which markedly impact the control design process. We also identify suitable actuator and sensor architectures with the sensor choice being depending on the nonlinear aeroelastic model characteristics. This controller is initially validated using a linear full-order model and then tested in a nonlinear simulation environment. While the controller fulfills the load alleviation and stabilization requirements, a reduced controller performance is observed with the higher-fidelity model in the loop necessitating a thorough reevaluation and adjustment of the control strategy in this computationally demanding setting.

1 INTRODUCTION

The aviation industry is a sector that is considered to be difficult to decarbonize and contributes $2 - 3\%$ to the global CO_2 emissions [1]. To reach the targeted net-zero eimissions until 2050, cutting-edge technological advancements are required and within the range of technologies explored, higher-aspect-ratio wings stood out to be one of the promising concepts to achieve significant fuel efficiency improvements. Increasing the aspect-ratio of the wing, decreases the induced drag, resulting in a higher lift-to-drag ratio, and thus, in a longer flight range and higher fuel efficiency. This concept is well known, and advances in composite materials in the past years have enabled significantly higher aspect ratios as they can keep the structural weight much lighter [2]. The resulting high-aspect ratio designs are naturally more flexible. This higher flexibility makes the air vehicle more susceptible to aeroelastic instabilities like flutter, as well as to higher expected wing loads during gust encounters and flight maneuvers. Further, this reduced structural stiffness results in elastic frequencies which might then no longer be distinctly differentiated from the frequencies of flight dynamics. This potential dynamic elastic/rigid coupling may need to be considered in high-aspect-ratio wing designs and certification of future commercial air vehicles, especially active control systems (ACS) are getting

involved [3, Chapter 1.3]. In this work, we focus on gust load alleviation (GLA) systems as an ACS which improves airframe design efficiency by using control surfaces to manipulate wing loads in real-time. This concept was already introduced in the early 1970s on the Lockheed C-5A and has been incorporated on the flying quality enhancement systems of the A380, A330, and B787 families [4]. IATA's current forecast [5] is for further evolution of the GLA technology to bring up to 5% additional fuel efficiency gains. However, this particular technology is strongly synergetic with the aerodynamic improvements from future high aspect-ratio wing designs, and the compound effect may have a much larger benefit. For example, the X-56A prototype aircraft claims around 30% reduction in structural weight through advanced use of GLA systems [6].

The higher flexibility of these high aspect-ratio wings is also addressed in recent GLA studies. An LQG controller for GLA has been designed and tested with a computational ASE model as a preparation for an upcoming transonic wind tunnel tests on the flexible, aspect ratio 13.5 Common Research Model (CRM) wind-tunnel model [7]. Static Output Feedback (SOF) controllers have been tested experimentally by Ricci et al [8] for GLA on a scaled, half-model reference regional aircraft, equipped with a flexible wing and a fuselage capable of free plunge and pitch motion. Poussot-Vassal et al [9] have designed a GLA controller using the H_∞-controller. For the control synthesis, a reduced-order version of a rational aeroservoelastic (ASE) model has been used and subsequently tested on first, a linear dynamical model of the Dassault Aviation generic ASE BizJet model /simulator and second, a 2D aeroservoelastic wind tunnel model at sub- and transonic speed. De Souza et al [10] designed a robust observer combined with a structured H_∞-controller using a reduced-order model obtained from a high-fidelity ASE wing-tail model. Another GLA design is to utilize feedforward control architectures for which in addition to local sensors, light detection and ranging (LIDAR) sensors detect atmospheric turbulence upstream of an aircraft [4]. Fournier et al [11] have employed a combined H_∞- and $\mathcal{H}_2$-controller within a preview control-architecture using a LIDAR focusing on the control robustness of GLA systems. Ting, Mesbahi, and Livne [12] have designed both a $\mathcal{H}_2$ and $\mathcal{H}_\infty$ preview controller, for GLA and evaluated their performance in wind tunnel tests, carried out with a flexible wing-body-tail model.

To sum up, many GLA systems have been designed for various flexible aircraft models using different control architectures. The similarities are mostly based on using linear (reduced-order) dynamic ASE models, mostly obtained from a linearization around a nonlinear equilibrium, for control design which is a natural choice. By relying solely on linear systems in the control performance evaluation, we may overlook important complex dynamics introduced by large (potentially geometrically nonlinear) deformations [3, Ch. 9]. For this, valuable insights can be gained from control schemes demonstrated with higher-order ASE models as hardware-in-the-loop systems. Specifically, Artola et al [13] have presented a framework for real-time control algorithm implementations based on fully nonlinear ASE simulations applied to stabilisation problems of a very-flexible aircraft. Similarly, Pereira et al [14] have developed an ASE framework for a flexible aircraft, focusing on a more accurate aerodynamic modelling for the final control application. Waite et al [15] have demonstrated a viable linear-quadratic Gaussian (LQG) controller, intended for active flutter suppression in wind tunnel experiments. They have examined the control performance on an ASE model including an unsteady Reynolds-averaged Navier-Stokes (RANS) aerodynamic solver, while for the structural dynamics, a modal solver has been used.

We aim to build a generic environment for control design and testing of low-speed flexible

vehicles, which is used in this work to investigate advanced GLA systems designed for a representative configuration of a more flexible aircraft for which some nonlinear phenomena become apparent. We especially focus on geometrically nonlinear effects becoming apparent for large deformation of the structure and gyroscopic effects due to stronger rigid/elastic couplings. In the present work, we use the LQG control scheme, which is a well-established control strategy and a compelling choice for GLA on (nearly Gaussian) atmospheric turbulence. The resulting framework is then used, first, to design such a controller and, second, to assess the control performance in more realistic simulations, especially by accounting for geometrically nonlinear effects.

The paper is structured such that we present the numerical methods used for the fully nonlinear aeroelastic simulations as well as the linearization and order-reduction process in section 2. Next, we propose the architecture of the control framework, outlining its necessary components and interfaces (section 3) and we introduce the flexible aircraft model in section 4. Subsequently, we discuss the control design process obtained in a linear environment and its gust alleviation capabilities in section 5. Finally, we put the designed controller in closed-loop with nonlinear aeroelastic simulations to evaluate the control performance (section 6).

2 AEROELASTIC COMPUTATIONAL METHODS

The nonlinear aeroelastic simulations are performed with the open-source simulation environment SHARPy [16]. SHARPy couples a nonlinear, displacement-based, geometrically-exact composite beam model (GEBM), capturing the structural dynamics, and unsteady vortex lattice method (UVLM) for the aerodynamics. Both GEBM and UVLM are presented in this section together with the linearization and reduction methodologies necessary for the later control design synthesis.

2.1 Structural Dynamics Solver

The primary structure of the aircraft is represented by geometrically nonlinear composite beams discretized in quadratic (3-node) finite elements [17, 18] and parametrized by nodal displacements and rotations, denoted by $\boldsymbol{\eta}$ within a body-attached FoR B. These beams are modelled by the GEBM which is a geometrically nonlinear formulation with nonlinear relationships for velocity and displacement kinematics whilst maintaining linear constitutive relations. Moreover, it accounts for follower forces by expressing them in a local structural frame of reference (FoR) S. The different FoRs are illustrated in Fig. 1 with the S-frame moving and rotating with the structure.
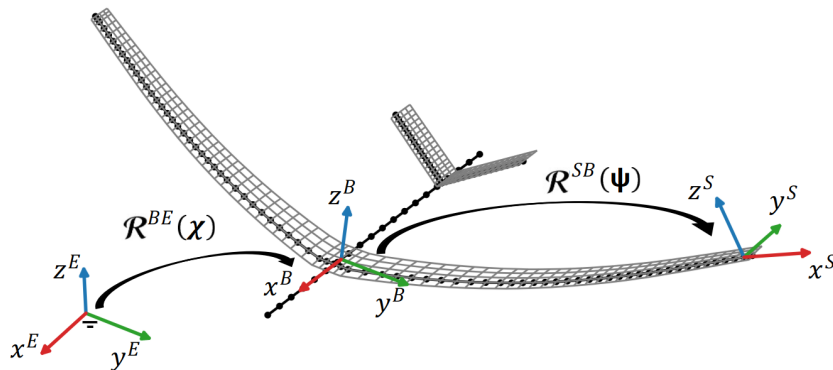

Figure 1: Illustration of the frames of reference as well as the structural and aerodynamic model of an aircraft.

The transformation from the B to the S-frame is obtained from the transformation matrix $\boldsymbol{\mathcal{R}}^{SB}$ using Cartesian rotation vectors, denoted by $\boldsymbol{\Psi}$, associated with each individual beam node. The B-frame moves with an instantaneous translational and angular velocity, denoted by $\boldsymbol{v}_B$ and $\boldsymbol{\omega}_B$, respectively, with respect to an inertial FoR E, which defines the rigid-body degrees of freedom (DoF) $\boldsymbol{\beta} = \begin{pmatrix} \boldsymbol{v}_B^\top & \boldsymbol{\omega}_B^\top \end{pmatrix}$. The orientation of the body-attached frame B to frame E is obtained from another transformation matrix $\boldsymbol{\mathcal{R}}^{BE}$ using quaternions $\boldsymbol{\mathcal{X}} = \begin{pmatrix} \mathcal{X}_0 & \boldsymbol{\mathcal{X}}_1^\top \end{pmatrix}^\top$. Quaternions and angular velocity are directly related by the attitude propagation equations allowing a simple integration to compute the vehicle orientation with [19]

$$\frac{d}{dt} \begin{bmatrix} \mathcal{X}_0 \\ \boldsymbol{\mathcal{X}}_1 \end{bmatrix} = \frac{1}{2} \begin{bmatrix} 0 & \boldsymbol{\omega}_B^T \\ \boldsymbol{\omega}_B & \tilde{\boldsymbol{\omega}}_B \end{bmatrix} \begin{bmatrix} \mathcal{X}_0 \\ \boldsymbol{\mathcal{X}}_1 \end{bmatrix}. \tag{1}$$

Finally, we apply Hamilton's principle to obtain the beam dynamics whose nonlinear form is

$$\boldsymbol{\mathcal{M}}(\boldsymbol{\eta}) \begin{bmatrix} \ddot{\boldsymbol{\eta}} \\ \dot{\boldsymbol{\beta}} \end{bmatrix} + \begin{bmatrix} \boldsymbol{\mathcal{N}}_{\text{gyr}}^S(\boldsymbol{\eta}, \dot{\boldsymbol{\eta}}, \boldsymbol{\beta}) \\ \boldsymbol{\mathcal{N}}_{\text{gyr}}^R(\boldsymbol{\eta}, \dot{\boldsymbol{\eta}}, \boldsymbol{\beta}) \end{bmatrix} + \begin{bmatrix} \boldsymbol{\mathcal{N}}_{\text{stiff}}^S(\boldsymbol{\eta}) \\ \boldsymbol{0} \end{bmatrix} = \begin{bmatrix} \boldsymbol{\mathcal{N}}_{\text{ext}}^F(\boldsymbol{\eta}, \dot{\boldsymbol{\eta}}, \boldsymbol{\beta}, \boldsymbol{\mathcal{X}}) \\ \boldsymbol{\mathcal{N}}_{\text{ext}}^R(\boldsymbol{\eta}, \dot{\boldsymbol{\eta}}, \boldsymbol{\beta}, \boldsymbol{\mathcal{X}}) \end{bmatrix} \tag{2}$$

with the mass matrix $\boldsymbol{\mathcal{M}}$ and gyroscopic, stiffness, and external generalised forces $\boldsymbol{\mathcal{N}}$. $\boldsymbol{\mathcal{N}}^F$ considers the forces and moments at the flexible DoFs and $\boldsymbol{\mathcal{N}}^R$ the rigid body ones. Both the inertial and elastic forces are nonlinear in Eq. 2 which is solved iteratively with a Newton-Raphson scheme, while an explicit, incrementally formulated Newmark-β scheme [20] is used for the time integration.

2.2 Unsteady Aerodynamic Solver

The GEBM is strongly coupled at each time step with the UVLM as an aerodynamic solver which is based on potential flow and thin wing theory. The UVLM predicts unsteady aerodynamic loads for three-dimensional low-speed and attached flow over thin lifting surfaces [21]. These surfaces are modelled as a lattice of quadrilateral panels whose corner points are aggregated into a column matrix $\boldsymbol{\zeta}(t)$. Each panel is associated with a bound vortex ring (index b) with a circulation, denoted by Γ_b. Another grid of unbound vortex rings captures the wake (index w), which is formed due to vortex shedding generated to satisfy the Kutta-Joukowski condition at the trailing edge and the Kelvin theorem [22]. The wake vortex rings convect with the background flow field that includes atmospheric disturbances. Control surfaces are modelled by deflecting the corresponding panels and, thus, affecting the aerodynamics.

Once the geometry is established and the singularity elements are positioned on both the lifting surface and wake panels, the induced velocity field at an arbitrary point in space $\boldsymbol{r}$ can be computed from

$$\boldsymbol{u}(\boldsymbol{r}, t) = \boldsymbol{\mathcal{A}}_b(\boldsymbol{r}, \boldsymbol{\zeta}(t))\boldsymbol{\Gamma}_b(t) + \boldsymbol{\mathcal{A}}_w(\boldsymbol{r}, \boldsymbol{\zeta}(t))\boldsymbol{\Gamma}_w(t) \tag{3}$$

with the aerodynamic influence coefficient (AIC) matrices $\boldsymbol{\mathcal{A}}_b$ and $\boldsymbol{\mathcal{A}}_w$. The AICs contain the normal velocity component $\boldsymbol{u}(\boldsymbol{r}_{ij}, t) \cdot \boldsymbol{n}_j$ on a collocation point, located at the center of panel j with its normal vector $\boldsymbol{n}_j$, induced by the vortex ring placed on panel i, where $\boldsymbol{u}(\boldsymbol{r}_{ij}, t)$ is calculated by Biot-Savart's law. After enforcing the non-penetrating boundary condition on each collocation point j, considering any external velocities (freestream velocity and gust velocities $\boldsymbol{w}_g$), we obtain a linear set of equations whose solution gives the circulation strengths $\boldsymbol{\Gamma}_b$ and $\boldsymbol{\Gamma}_w$. From these circulation strengths, we compute the resulting aerodynamic forces using the unsteady Kutta-Joukowsky theorem [23]. Vortex rings induce a quasi-stationary force that takes into account the suction effect of the leading edge, and an unsteady force that incorporates the additional mass effect [24].

This aerodynamic model has recently been enhanced in Ref. [25] by, first, fuselage aerodynamics by coupling a linear source panel method coupled with this UVLM, second, sectional airfoil polar corrections that are incorporated on the aerodynamics under potentially large deformations, and third, a new wake discretization scheme accelerating the presented UVLM simulations.

Control surfaces are modeled by allowing deflection of the corresponding panels, thus affecting the aerodynamics. Further note that the changes in aerodynamic forces due to control surface deflections are expected to be slightly overestimated as a result of the underlying potential flow characteristics.

2.3 Linear System Assembly and Reduction Methodologies

We continue with the description of the linearization and order-reduction process of a nonlinear aeroelastic system. For this system, we first compute the nonlinear aeroelastic equilibrium with the previously presented nonlinear solver. The model is then linearized around this equilibrium with its reference conditions denoted by the subscript $(\cdot)_0$.

The linearization is carried out for the UVLM and GEBM individually and we begin with the description of the GEBM linearization. This linearization of the nonlinear structural dynamics, formulated in equation (2), is linearized based on the identical reference equilibrium state. For this equilibrium, we know that both structural velocities and accelerations are zero, i.e. $\ddot{\boldsymbol{\eta}}_0$ and $\dot{\boldsymbol{\beta}}_0$, and that the external forces must be in balance with the stiffness and gyroscopic forces, i.e. $\boldsymbol{N}_{gyr}(\boldsymbol{\eta}, \dot{\boldsymbol{\eta}}, \boldsymbol{\beta}) + \boldsymbol{N}_{stiff}(\boldsymbol{\eta}) = \boldsymbol{N}_{ext}(\boldsymbol{\eta}, \dot{\boldsymbol{\eta}}, \boldsymbol{\beta}, \boldsymbol{\mathcal{X}})$. With these conditions for the equilbrium state, we can perturbate the GEBM model from Eq. 2 assuming small amplitudes, resulting in the perturbation equations [19]

$$\boldsymbol{\mathcal{M}}(\boldsymbol{\eta}_0) \begin{bmatrix} \Delta\ddot{\boldsymbol{\eta}} \\ \Delta\dot{\bar{\boldsymbol{\beta}}} \\ \Delta\dot{\boldsymbol{\Theta}} \end{bmatrix} + \boldsymbol{\mathcal{C}}(\boldsymbol{\eta}_0, \dot{\boldsymbol{\eta}}_0, \boldsymbol{\beta}_0) \begin{bmatrix} \Delta\dot{\boldsymbol{\eta}} \\ \Delta\boldsymbol{\beta} \\ \Delta\boldsymbol{\Theta} \end{bmatrix} + \boldsymbol{\mathcal{K}}(\boldsymbol{\eta}_0, \dot{\boldsymbol{\eta}}_0, \boldsymbol{\beta}_0) \begin{bmatrix} \Delta\boldsymbol{\eta} \\ 0 \\ 0 \end{bmatrix} = \begin{bmatrix} \Delta\boldsymbol{\mathcal{N}}_{ext}^S(\Delta\boldsymbol{\eta}, \Delta\dot{\boldsymbol{\eta}}, \Delta\boldsymbol{\beta}, \Delta\boldsymbol{\Theta}) \\ \Delta\boldsymbol{\mathcal{N}}_{ext}^R(\Delta\boldsymbol{\eta}, \Delta\dot{\boldsymbol{\eta}}, \Delta\boldsymbol{\beta}, \boldsymbol{\Theta}) \\ 0 \end{bmatrix}$$

$$(4)$$

The state variables comprise the flexible degree of freedom (DoF) deviations $\Delta\boldsymbol{\eta}_i$ for each node i, their gradient $\Delta\dot{\boldsymbol{\eta}}_i$, and the deviations of the rigid body. These rigid body perturbations include the orientation, defined using the immediate translational and rotational velocities of the B-frame and Euler angles. These Euler angles, denoted by $\boldsymbol{\Theta} = [\phi, \theta, \psi]$ for roll, pitch, and yaw, replace the quaternions $\boldsymbol{\mathcal{X}}$ as a parametrisation in the linear model. Lastly, $\Delta\bar{\boldsymbol{\beta}}$ is the integro-state (quasi-coordinates) associated with the velocities of the rigid body to separate the displacement and velocity modes.

We further reduce the linear structural system by projecting it onto the modal coordinates of the deformed system. This modal projection expressed as

$$\begin{bmatrix} \Delta\boldsymbol{\eta} \\ \Delta\bar{\boldsymbol{\beta}} \\ \Delta\boldsymbol{\Theta} \end{bmatrix} = \boldsymbol{\Phi}\Delta\boldsymbol{q}, \qquad \begin{bmatrix} \Delta\dot{\boldsymbol{\eta}} \\ \Delta\boldsymbol{\beta} \\ \Delta\boldsymbol{\Theta} \end{bmatrix} = \boldsymbol{\Phi}\Delta\dot{\boldsymbol{q}}, \text{ and} \qquad \begin{bmatrix} \Delta\ddot{\boldsymbol{\eta}} \\ \Delta\dot{\bar{\boldsymbol{\beta}}} \\ \Delta\dot{\boldsymbol{\Theta}} \end{bmatrix} = \boldsymbol{\Phi}\Delta\ddot{\boldsymbol{q}}. \qquad (5)$$

is obtained by computing $\boldsymbol{\Phi}$ from solving the eigenvalue problem by substituting Eq. (4) into the equations above. The modal displacement field $\boldsymbol{q}$ and the resulting modal velocities $\dot{\boldsymbol{q}}$ then describe the structural dynamics. This system can be truncated to a suitable number of modes n_q that capture the most important dynamics for the given system [26].

Subsequently, we linearize the UVLM which is performed analytically, assuming constant AICs and a frozen wake shape while including steady load effects. This yields a discrete, linear time-invariant (DLTI) system in state-space as demonstrated by Maraniello and Palacios [27]. This DLTI system of the UVLM has been further adapted, as described in Ref. [26], by first, mapping the linear control surface deflections $\boldsymbol{\delta}$ and their rates $\dot{\boldsymbol{\delta}}$ onto the deformed vortex lattice grid described by $\boldsymbol{\zeta}$ and $\dot{\boldsymbol{\zeta}}$. Second, the gust inputs which map three-dimensional velocity vectors to each vortex-ring panel, leading to a high number of inputs, are reduced to a single gust input. This input describes the vertical velocity at the foremost leading edge and is then mapped to any lattice grid point $\boldsymbol{\zeta}$ considering a convection of this gust velocity downstream with the freestream velocity (as does any disturbance in the UVLM) using a linear interpolation approach.

The final augmented DLTI UVLM is written as

$$\boldsymbol{x}_a(k+1) = \boldsymbol{A}_a\boldsymbol{x}_a(k) + \boldsymbol{B}_a\boldsymbol{u}_a(k) \tag{6}$$

$$\boldsymbol{y}_a(k) = \boldsymbol{C}_a\boldsymbol{x}_a(k) + \boldsymbol{D}_a\boldsymbol{u}_a(k)\,, \tag{7}$$

The output is composed of the dimensionless forces, including steady and unsteady components, at these vertices, and is written as $\boldsymbol{y}_a(k) = \Delta\boldsymbol{F}(k)$. The inputs include $\boldsymbol{u}_a(k) = \left[\Delta\boldsymbol{\zeta},\ \Delta\dot{\boldsymbol{\zeta}},\ \Delta\boldsymbol{w}_g,\ \Delta\boldsymbol{\delta},\ \Delta\dot{\boldsymbol{\delta}}\right]$ and the states $\boldsymbol{x}_a(k) = \left[\Delta\boldsymbol{x}_{w_g},\ \Delta\boldsymbol{\Gamma}_b,\ \Delta\boldsymbol{\Gamma}_w,\ h\Delta\dot{\boldsymbol{\Gamma}}_b,\ \Delta\boldsymbol{\Gamma}_b(k-1)\right]$. $\Delta(\cdot)$ denotes small perturbations around the reference, and the integers k and h are the current discrete time step and its size. Note that we omit specifying the discrete time step of an aeroelastic parameters if referring to the current time step to improve readability. The time-derivative $\dot{\boldsymbol{\Gamma}}$ is essential for capturing the added mass effects and is computed with second-order accuracy (thus $\Delta\boldsymbol{\Gamma}_b(k-1)$ as a state). Finally, the states $\boldsymbol{x}_{w_g}$ map the gust input at the foremost leading edge denoted by $\boldsymbol{w}_g$ to each individual vortex ring.

The DLTI UVLM system has usually states in the order $\mathcal{O}(10^4 - 10^6)$ because of the long and fine wake vortex lattice grid which is often essential for achieving convergence. Given this high number of states, the use of reduced-order models (ROM) is essential for the design of the controller and its subsequent application. Krylov subspace methods [28], implemented by Goizueta et al [26] into SHARPy, are especially advantageous for UVLM since these methods can match specifiable local regions of the system transfer function to include the important lower frequency spectrum, where the prevailing physics and core assumptions about potential flow lie [19].

Ultimately, the aerodynamic and structural dynamic systems, which were linearized separately, are coupled. In this process, the aerodynamic force output $\Delta\boldsymbol{F}$ stemming from the DLTI-UVLM system in the E-frame is projected onto the structural DoF in the S-frame. These transformed forces can then be input directly into the GEBM system as forces and moments, denoted by $\Delta\boldsymbol{\mathcal{N}}$, using linear mapping [19]. The GEBM system then yields the resulting grid geometries and velocities based on the subsequent node displacements and velocities, which then serve as inputs to the DLTI UVLM system. Lastly, we reduce the control inputs by assuming $\boldsymbol{\delta}(k+1) = \boldsymbol{\delta}(k) + h\dot{\boldsymbol{\delta}}(k)$ which allows us to express the control surface deflection $\boldsymbol{\delta}$ as a state.

The resulting linearized coupled aeroelastic system

$$\boldsymbol{x}_{ae}(k+1) = \boldsymbol{A}_{ae}\boldsymbol{x}_{ae}(k) + \boldsymbol{B}_{ae}\boldsymbol{u}_{ae}(k)$$
$$\boldsymbol{y}_{ae}(k) = \boldsymbol{C}_{ae}\boldsymbol{x}_{ae}(k) + \boldsymbol{D}_{ae}\boldsymbol{u}_{ae}(k)\,, \tag{8}$$

has now the following states, inputs, and outputs for the linear full-order model (FOM) system:

$$\boldsymbol{x}_{ae}(k) = \left[\Delta \boldsymbol{x}_{w_g}, \ \Delta \boldsymbol{\Gamma}_b, \ \Delta \boldsymbol{\Gamma}_w, \ h\Delta \dot{\boldsymbol{\Gamma}}_b, \ \Delta \boldsymbol{\Gamma}_b(k-1), \ \Delta \boldsymbol{q}, \ \Delta \dot{\boldsymbol{q}}, \ \Delta \boldsymbol{\delta} \right]$$

$$\boldsymbol{u}_{ae}(k) = \left[\Delta \boldsymbol{w}_g, \ \Delta \dot{\boldsymbol{\delta}} \right]$$

$$\boldsymbol{y}_{ae}(k) = \left[\Delta \boldsymbol{\mathcal{N}}, \Delta \boldsymbol{\eta}, \Delta \dot{\boldsymbol{\eta}}, \Delta \boldsymbol{\beta}, \Delta \boldsymbol{\Theta}, \Delta \ddot{\boldsymbol{\eta}}, \Delta \dot{\boldsymbol{\beta}}, \Delta \dot{\boldsymbol{\Theta}} \right] .$$

3 PROPOSED GLA CONTROL FRAMEWORK ARCHITECTURE

The proposed GLA control framework is depicted in Fig. 2 and uses SHARPy as a nonlinear aeroelastic hardware-in-the-loop simulator of a vehicle flying in a non-stationary atmosphere. From this system, we can extract various performance metrics and more importantly sensor measurements $\boldsymbol{y}$ that are sent from SHARPy using a User Datagram Protocol (UDP) interface to a controller deployed on a different platform, as described in Ref. [29]. Based on these readings, this controller then generates control inputs $\boldsymbol{u}$ that are fed back to the actuators of the nonlinear aeroelastic system using another UDP network. This network architecture is chosen to enable design freedom for future projects in terms of control architecture and software choice.

In this work, we have chosen the LQG controller that is run in Simulink. This controller is synthesised from a linear ROM that can be obtained from the linearization and reduction methods outlined in section 2.3. Simultaneously, both the linear FOM and ROM provide efficient modeling capabilities to fine-tune the controller before applying it to the more computational-intensive nonlinear aeroelastic model.

We continue this section with the formulation of the LQG controller and present appropriate gust models, serving as the disturbance input to our system.
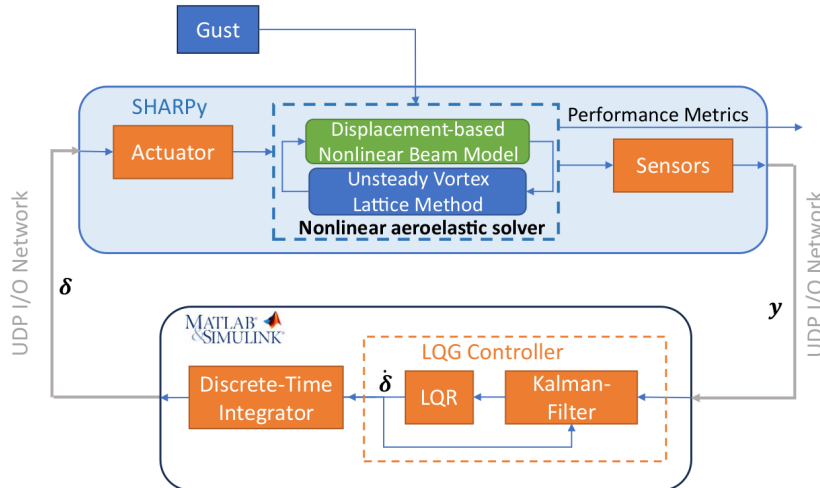

Figure 2: Outline of the GLA framework using SHARPy as a nonlinear aeroelastic hardware-in-the-loop simulator.

3.1 Linear Quadratic Gaussian Controller

The linear quadratic Gaussian (LQG) controller is an optimal sensor-based feedback controller that combines a linear quadratic regulator (LQR)-based state feedback controller with a Kalman filter for state estimation [30]. Each part can be designed separately exploiting the separation principle. To do so, the aeroelastic DLTI system in Eq. (8) already provides a starting point since it is written in the conventional state space form from linear control theory. This encompasses

the state $\boldsymbol{x}_{ae}$, input $\boldsymbol{u}_{ae}$, output $\boldsymbol{y}_{ae}$ as well as state space matrices $\boldsymbol{A}_{ae}, \boldsymbol{B}_{ae}, \boldsymbol{C}_{ae}$, and $\boldsymbol{D}_{ae}$. To simplify the notation, the subscripts ae are omitted.

We start with the description of the LQR controller which determines the (static) gain matrix $\boldsymbol{K}_r$ for the control law

$$\boldsymbol{u}(k) = -\boldsymbol{K}_r \boldsymbol{x}(k)\,, \tag{9}$$

by minimizing the cost function

$$J_{LQR}(\boldsymbol{u},\, \boldsymbol{x}(0)) = \frac{1}{2}\sum_{k=0}^{\infty}\boldsymbol{x}^{\top}(k)\boldsymbol{Q}\boldsymbol{x}(k) + \boldsymbol{u}^{\top}(k)\boldsymbol{R}\boldsymbol{u}(k)\,. \tag{10}$$

The matrices $\boldsymbol{Q}$ (positive semi-definite) and $\boldsymbol{R}$ (positive definite) weigh both the cost of deviations from the reference condition and the cost of the actuation, respectively. These matrices define a compromise between the required control effort and the desired closed-loop performance along with the relative weighting of the different states and control input channels, accounting for a change in coordinates. The resulting control law, henceforth referred to as the LQR controller, is of the form (9), where the optimal gain is given by $\boldsymbol{K}_r = (\boldsymbol{R} + \boldsymbol{B}^{\top}\boldsymbol{P}\boldsymbol{B})^{-1}\boldsymbol{B}\boldsymbol{P}\boldsymbol{A}$, with $\boldsymbol{P}$ being the (stabilising) solution of the discrete-time algebraic Riccati equation [31, Chapter 8.3].

A common state-estimator paired with the LQR is the Kalman filter [32–34] which estimates the full-state $\boldsymbol{x}$ from noisy sensor measurements. This filter takes into account both disturbance and output noise, denoted by $\boldsymbol{w}_d$ and $\boldsymbol{w}_n$, respectively, and it is the optimal estimator for the case in which these noises are uncorrelated zero-mean Gaussian processes. This makes the LQG controller an interesting choice for GLA due to the common assumption of Gaussian turbulence (e.g. von Kármán turbulence model). The covariances of these noises determine the filter parameters $\boldsymbol{K}_f$. The underlying dynamics of the Kalman filter can be expressed as

$$\hat{\boldsymbol{x}}(k+1) = \boldsymbol{A}\hat{\boldsymbol{x}}(k) + \boldsymbol{B}\boldsymbol{u}(k) + \boldsymbol{K}_f(\boldsymbol{y}(k) - \hat{\boldsymbol{y}}(k)) \tag{11}$$

$$\hat{\boldsymbol{y}}(k) = \boldsymbol{C}\hat{\boldsymbol{x}}(k) + \boldsymbol{D}\boldsymbol{u}(k) \tag{12}$$

with the estimated state and output denoted by $\hat{\cdot}$. As in the case of the LQR controller, the gain matrix $\boldsymbol{K}_f$ is given by the solution of a discrete-time algebraic Riccati equation.

Finally, the LQG controller is obtained by combining the Kalman filter with the LQR, which results in the control law given by

$$\boldsymbol{u}(k) = -\boldsymbol{K}_r\hat{\boldsymbol{x}}(k)\,. \tag{13}$$

The resulting dynamic system can be written as

$$\dot{\boldsymbol{x}}(k+1) = (\boldsymbol{A} - \boldsymbol{K}_f\boldsymbol{C} - \boldsymbol{B}\boldsymbol{K}_r)\hat{\boldsymbol{x}}(k) + \boldsymbol{K}_f\boldsymbol{y}(k) \tag{14}$$

combined with the filter dynamics described by equations (11) and (12). The cost function of the LQG controller is an ensemble-averaged version, or the expected value, of the LQR cost function [30]

$$J_{LQG}(\boldsymbol{u}, \boldsymbol{x}(0)) = \frac{1}{2}\left\langle \sum_{k=0}^{\infty}\boldsymbol{x}^{\top}(k)\boldsymbol{Q}\boldsymbol{x}(k) + \boldsymbol{u}^{\top}(k)\boldsymbol{R}\boldsymbol{u}(k)\right\rangle \tag{15}$$

with $\langle\bullet\rangle$ indicating the expected value of variable $\bullet$.

3.2 Gust Modelling

The disturbance input is the time history of gust velocities in our cases. In this work, we are using the gust models part of current airworthiness regulations by EASA [35] and FAA [36], namely the discrete 1-cosine gust and continuous turbulence model, where the latter is based on the von Kármán spectrum.

The mathematical expression of the 1-cosine gust can be written as

$$w_{g,z} = U_{ds} \cdot \left(1 - \cos\left(\frac{\pi x^E}{H} \right) \right) . \tag{16}$$

The spatial coordinate x^E is expressed in the inertial FoR and is parallel to the initial flight direction of the aircraft. The design gust velocity U_{ds} defines the maximum gust velocity and the distance between the gust onset and this maximum is defined by the gust length H.

This discrete gust model is a sufficient representation to compute the gust-induced wing loads, especially for short gusts of large amplitude as observed by flight data [37]. However, to more accurately capture the random and continuous characteristics of an atmospheric turbulence field during gust encounters, the continuous gust, or continuous turbulence, model becomes essential. This model's turbulent velocity field can be generated from the von Kármán spectrum that defines linear and angular velocity components of the gust by a power spectral density (PSD) function with the vertical component of the PSD Φ_{w_g} defined as

$$\Phi_{w_g}(\kappa) = \sigma_w^2 \frac{L_g}{\pi} \frac{1 + \frac{8}{3}(1.339\,L_g\,\kappa)^2}{[1 + (1.339\,L_g\,\kappa)^2]^{11/6}} . \tag{17}$$

Here σ_w is the root-mean-square of the turbulent velocity (in ft/s), L_g the gust length scale, specified by the FAA as 2500 ft [36], and κ is the wavenumber. The spatial profile of the gust is generated from the spectrum using a turbulence filter assuming a constant flight velocity [3, Ch. 2]. Both the discrete and continuous gust are frozen in space and the velocity field only varies along the spatial coordinate x^E, i.e. is not affected by large altitude changes.
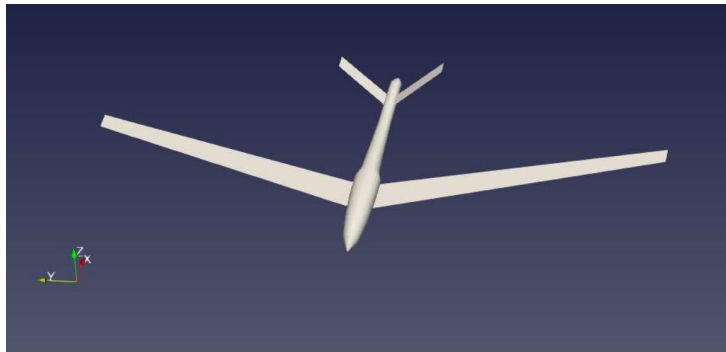
4 REPRESENTATIVE AIRCRAFT DEMONSTRATOR

Figure 3: Three-dimensional visualization of the SuperFLEXOP aerodynamic model in SHARPy.

We exercise the capabilities of the proposed GLA control framework architecture on the SuperFLEXOP, illustrated in Fig. 3, which is a representative aircraft based on a more flexible version of the FLEXOP UAV with the wing mass and stiffness properties of Sodja et al [38]. As their wing model is based on an earlier rather stiff version, we reduced the original stiffness by scaling the stiffness matrix by 0.3, resulting in a $6.2\,\%$ instead of a $2.3\,\%$ wingtip deformation in forward flight. We refer to this model henceforth as the SuperFLEXOP.

4.1 Model Setup

The SuperFLEXOP features a tapered and swept wing, a V-tail, and a fuselage. The details for the reference wing have been kindly provided by Sodja et al [38] and include spanwise varying mass and (later scaled) stiffness beam properties, jig twist, shear centre, airfoil geometry, lumped mass distribution, and other main geometrical parameters. The latter are summarized in Table 1 together with the V-tail dimensions. The V-tail and fuselage dimensions are both are extracted from CAD sketches sourced from [39]. The fuselage has a length of 3.44 m and the nose-wing and nose-tail offsets are 0.884 m and 2.86 m, respectively.

Further assumptions for the V-tail and fuselage components are no significant flexibility, enforced by stiffness values much higher than the wing, as well as a realistic mass distribution of m̄ of 1.2 kg·m^{-1} for the V-tail and 3.0 kg·m^{-1} for the fuselage. The cross-sectional inertia is assumed to be $J = 0.1$ kg·m.

A payload of 31.3 kg is added at 1.36 m aft the nose to match the centre of gravity position specified in [40] and specified takeoff weight of 65.4 kg [38] which results also from the total structural mass of the tail (2.0 kg), fuselage (10.3 kg), and wing (11.5 kg) as well as the 10.3 kg, coming from lumped masses attached to the latter.

The described implemented model has already been verified in [25] by firstly comparing the steady-state spanwise wing deformation and load distribution and secondly the modal frequencies under wind-off conditions. This comparison has been made using the original stiffness values with the reference model [38] showing good agreement.

4.2 Controllability

The model is equipped with four ailerons on each wing and two elevators on each V-tail surface, as depicted in Fig. 4, utilizing geometrical dimensions specified for the ailerons in [38] and assumed for the elevators. These control surfaces serve both for load alleviation and the elevator is additionally deployed for cruise flight trimming. The deflection and deflection rate limits are set at $\delta_{max} = \pm 25$ deg and $\dot{\delta}_{max} = \pm 50$ deg/s, with positive values indicating downward deflection. Please note that these constraints are not yet fully representative of real actuator behaviour and have not been rigorously enforced, but are deemed to be appropriate for the current proof of concept of controller design.

4.3 Flight and Structural Dynamic Characteristics

The stiffness modification, leading to the SuperFLEXOP model, not only results in higher wing deformations but also alters the dynamic response of the vehicle. More precisely, the wing modal frequencies scale with the square root of the scaling factor of 0.3 since the inertia properties are not modified.

Table 1: Overview of the main geometry parameters defining the SuperFLEXOP model.

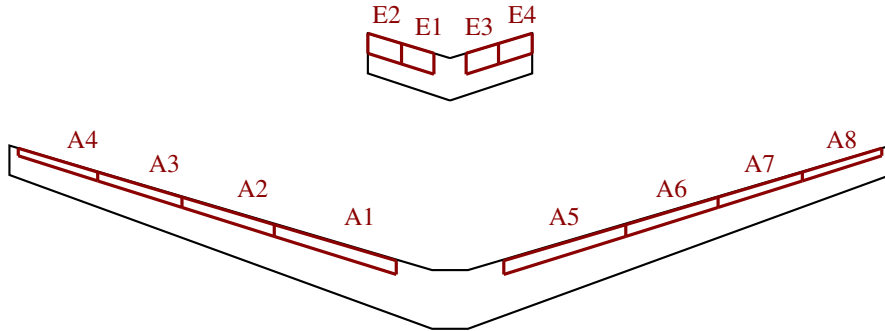| Parameter	Wing	Tail
span	7.07 m	1.32 m
sweep	20 deg	18 deg
chord root/tip	0.471 m/0.236 m	0.217 m / 0.180 m
opening angle	0 deg	35 deg
airfoil	custom [38]	NACA0012

Figure 4: Control surface layout of the SuperFLEXOP model.

While this scaling led to the desired structural torsional and out-of-plane (OOP) bending behavior, the more flexible in-plane (IP) bending behavior of the wing led to several issues when incorporating the LQG controller for the closed-loop simulations of the SuperFLEXOP's nonlinear gust response behavior. These issues are explained in more detail in section 6. For this reason, the IP stiffness of the wing structure was increased by $60\,\%$ which barely affected the OOP bending and torsional modes. The resulting structural modal frequencies of the wing and the full SuperFLEXOP configuration are summarized in Table 2.

Table 2: Modal frequencies in Hz and identified mode shapes of the trimmed SuperFLEXOP.

Mode	Clamped	Free-Flying	
	-	symmetric	asymmetric
1st OOP bending	3.15	3.40	5.82
2nd OOP bending	9.00	9.34	14.42
3rd OOP bending	19.41	19.77	24.72
4th OOP bending	29.83	30.02	31.77
1st Torsion	39.58	38.83	45.0
5th OOP bending	51.62	51.67	51.68
6th OOP bending	63.37	63.44	62.25
2nd Torsion	65.30	65.47	69.78

5 CONTROL DESIGN OF THE GLA SYSTEMS

This section describes the control design for a GLA controller applied to the SuperFLEXOP, which must first be linearized around its nonlinear aeroelastic equilibrium. This full-order linear model (FOM) is subsequently reduced using Krylov-based methods, resulting in a reduced-order linear model (ROM). The linearization of the SuperFLEXOP has been verified in Ref. [29], indicating an overestimation of the peak wingtip displacement by around $3\,\%$ and $4\,\%$ with the linear FOM of the clamped and free-flying SuperFLEXOP, respectively. The reason being is that the geometric stiffening of the structure is not captured with the linear FOMs. The order-reduction methods have been verified in Ref. [41], indicating an accurate capture of the flight dynamics by the ROM compared to the FOM. We next design the LQG controller components, i.e. the LQR controller and the Kalman Filter.

5.1 LQR Design

We start by assuming available full-state measurements to design the LQR, while the state-estimation done by the Kalman-Filter will be subject of the following section. The LQR design includes choosing the weight matrix $\boldsymbol{Q}$ and cost matrix $\boldsymbol{R}$ to tune the closed-loop gust response of the aircraft with the objectives to 1) alleviate the gust-induced wingtip displacement (pro-

portional to the wing root bending moments, 2) avoid control surface saturation limits, and 3) ensure flight stability. During the design process, substantial differences have been observed for the closed-loop response of the clamped and free-flying SuperFLEXOP. The main reason for this is the strong coupling of structural and rigid body modes that have already been observed in the open-loop gust response. Thus, we discuss the control designs for both configurations separately, starting with the clamped wing.

5.1.1 Clamped SuperFLEXOP wing

The linear ROM of the clamped SuperFLEXOP wing has 48 aerodynamic states and 24 structural states including the modal displacement and velocities of the first to fifth OOP bending modes and the first torsional mode for each wing. We further have 8 states, representing the aileron deflections $\boldsymbol{\delta}_A$ for the control surfaces on each wing, resulting in a total of 80 states. The ROM further has 8 inputs representing the aileron deflection rates $\dot{\boldsymbol{\delta}}_A$. Apart from the states $\boldsymbol{x}$, we further output the vertical wingtip displacement z_{tip} as a performance matrix as it correlates well with the wing root bending moment [29].

We impose no penalty on the aerodynamic states since after the reduction process, these states do not preserve physical meanings as opposed to the structural modes which make the latter easier to interpret. A satisfying reduction in wingtip displacement is observed when penalizing the first modal displacement q_1 and velocity $\dot{q}_1$ which are linked to the first bending mode. For the clamped SuperFLEXOP wing, it was found that penalizing only the first modal displacement q_1 is sufficient enough and, thus, to keep the design simpler, only the diagonal weight for q_1 needs to be chosen. All other modes are not penalized as this does not improve the achieved wingtip displacement reduction of the actuator. Further, during this research project, penalizing higher modes can more easily introduce instabilities in case of wrong state estimations, especially of the IP bending mode, by the Kalman-Filter, which have been observed with the nonlinear FOM in closed-loop. Last, we penalize the control surface deflections of the ailerons to avoid saturated actuators and also speed up the return to the initial aileron deflections.

In a first case, we consider all ailerons to deflect the same, resulting in a single input single output (SISO) system. The cost matrix is held constant to $\boldsymbol{R} = \boldsymbol{I}$. The diagonal weights for q_1 and the aileron deflection states $\boldsymbol{\delta}$ have been tuned considering a trade-off between obtained wingtip deflection reduction and staying away from actuator saturation, with the final penalties chosen as 140 for q_1 and 50 for $\boldsymbol{\delta}$. The resulting LQR control performance can be observed from the time-history of the open- and closed-loop response of the clamped SuperFLEXOP wing, considering the linear FOM, to discrete 1-cosine gusts with considered gust lengths of $2H = 5 - 40\,\mathrm{m}$ and a maximum gust velocity is $U_{ds}/U_\infty = 0.1$. The resulting vertical tip deflections Δz_{tip}, normalized by the half wingspan b, as well as the aileron deflection and its rates are shown in Fig. 13.

The LQR controller in closed-loop with the linear FOM commands the aileron to deflect as expected downward to substantially reduce the gust-induced vertical wingtip displacement, namely relatively by $18.9\,\%$, $25.3\,\%$, $32.5\,\%$ and $37.11\,\%$ for the gust lengths in ascending order. For short gust lengths, the aileron deflection rate is quite high due to the faster gusts, giving the controller less reaction time to sufficiently reduce the gust-induced wingtip displacements without reaching saturation values. Hence, short gust lengths are limiting the penalty that can be imposed on q_1, directly constraining the GLA performance factor. As the gust length increases, the deflection rate decreases. The resulting aileron deflections $\boldsymbol{\delta}$ are all within reasonable limits and the maximum deflection increases in longer gust encounters due to higher deflections

associated with higher bending loads. The ailerons are already deflected prior to a noticeable wingtip deflection since the first modal displacement q_1 already increases noticeably by the gust hitting the swept wing further upstream, inducing torsional bending especially noticeable at the wingtip.
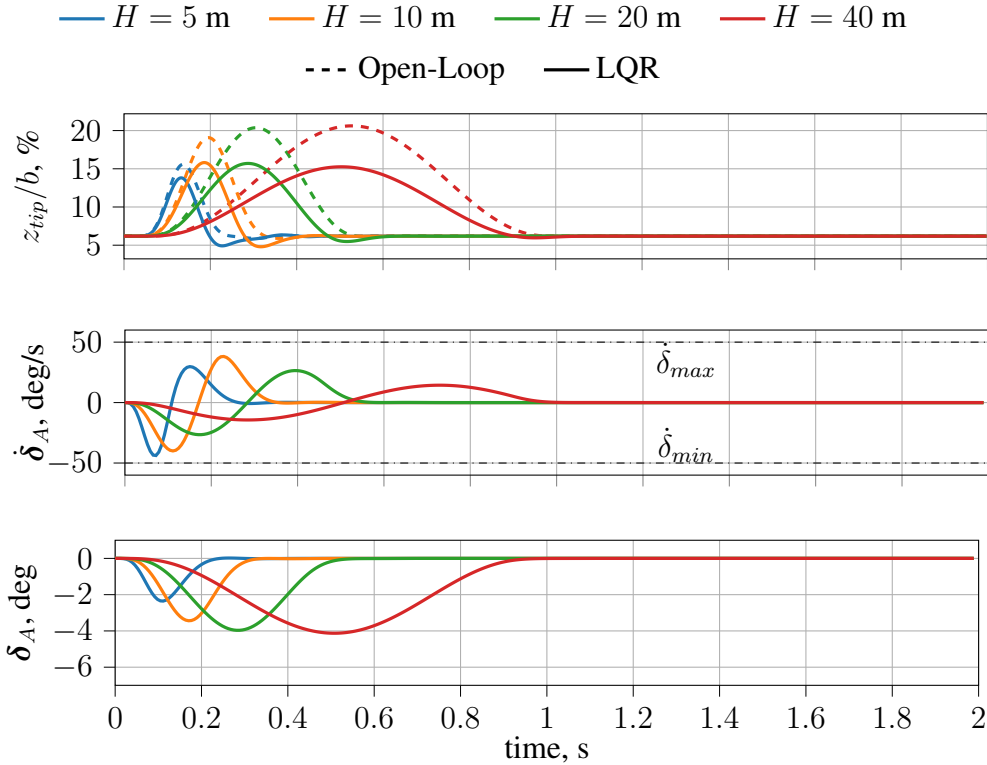

Figure 5: Closed-loop LQR gust response of the linear, clamped SuperFLEXOP wing to the 1-cosine gust with various gust lengths H.

Next, we deploy all ailerons individually. For the resulting multiple input single output (MISO) system, we have to adjust the weights for the first modal displacement q_1 again to a value of 400 to avoid saturation of the control surface deflection rate for short gust lengths, while preserving similiar closed-loop performance. The reason for this adjustment is necessary since, as expected, some ailerons are more effective than others for GLA. More precisely, we observe higher aileron deflections for the outboard-located ailerons. For a gust length of $H = 10\,\mathrm{m}$, we actually have a $52.7\,\%$ and $18.17\,\%$ less deflection of the innermost aileron and its adjacent one compared to the outermost loacted one. The second outermost aileron deflects $5.6\,\%$ more than the most-outboard one, and therefore appears to be the most effective aileron for reducing the gust-induced tip displacement of the wingtips in the present configuration. These aileron deflections scale similarly for various other gust lengths.

The effectiveness of the ailerons for GLA dependents on several factors. First, the more-inboard located ailerons have a smaller lever arm than the further-outboard ones. Thus, the local lift reduction has a smaller effect on both the wing-root bending moment and wingtip displacement. However, the torsional moments might increase more with the deflection of the further-outboard aileons. Second, outboard ailerons very close to the wingtip can suffer from lower control effectiveness or even control reversal as observed by Pusch et al. [42] and Stanford [43]. While the first point, describes the higher deflection for the outermost ailerons, the second point explains the higher effectivness of the second outermost aileron compared to the outermost one.

Next, we apply the designed LQR controllers, i.e. SI and MI, to alleviate a continuous gust over an extended period of $500\,\mathrm{s}$. For the SI-controller, we see in Fig. 6 a sufficient reduction in the peak displacements achieved by the LQR controller, which reduces the root mean square (RMS) of the wingtip displacement by $40.00\,\%$. The ailerons are far from the saturation values, both in terms of maximum deflection and speed. The results for the MI-controller are not included in this figure, as due to the strong fluctuations, the curves are hard to distinguish and thus, only a statistical evaluation is provided. For the MI-controller, we achieve with $37.15\,\%$ a comparable reduction in the RMS of the peak displacement. We see similiarities in the different actuator responses as in the discrete MI gust response. More precisely, the ailerons starting from inboard to outboard aileron have an RMS deflection rate relative for the SI case of $50.65\,\%$, $82.00\,\%$, $103.33\,\%$, and $96.62\,\%$. Comparable ratios result for the minimum and maximum deflection rates, and thus the deflections themselves as well.
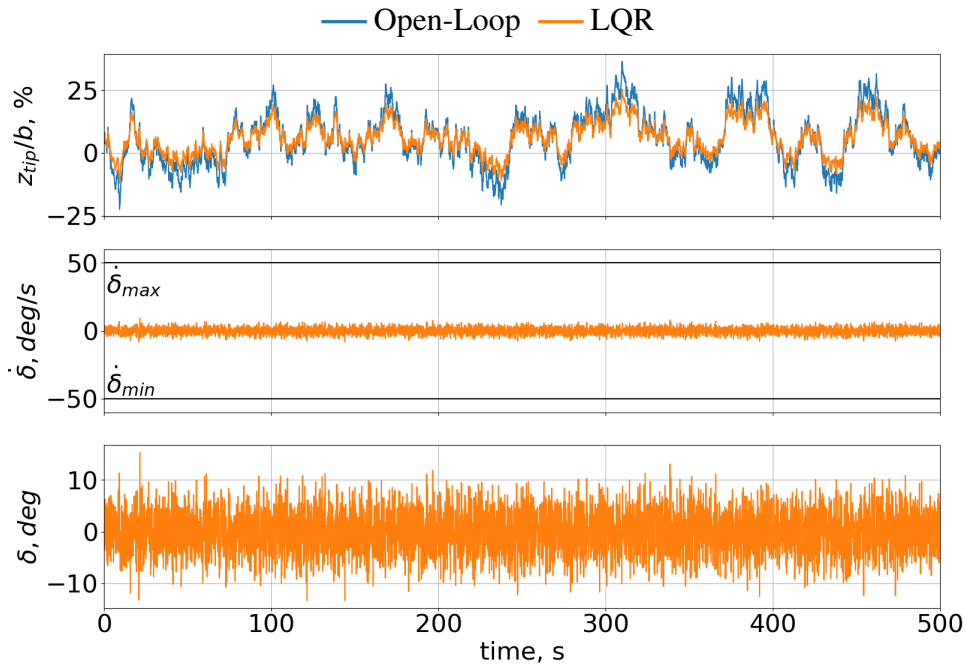
Figure 6: Closed-loop LQR gust response of the linear, clamped SuperFLEXOP wing to the continuous gust with $\sigma_w = 2.93$.

5.1.2 Free-Flying SuperFLEXOP

The linear ROM for the SuperFLEXOP considering rigid body motions has 72 aerodynamic states, 33 structural states, including 9 rigid body states, and 8 states corresponding to $\boldsymbol{\delta}$. We again start with a SI system, assuming joined ailerons. For the LQR design, similiar tuning strategy is used, with no penalties on the aerodynamic states, as well as structural states higher than one. The same penalty for $\boldsymbol{\delta}$ is used, i.e. 50. However, when again penalizing the first modal displacement with 0.4, the closed-loop performance does not fulfill the GLA objectives, as seen in Fig. 7, where the closed-loop performance of different LQR controllers are compared. The tip displacement is only reduced for short gust lengths, but for larger ones, we actually observe increased tip displacement as well as an enhanced rigid body response, as seen from stronger pitch down motions θ and larger peaks in the vertical velocity v_z^B. Further, this response causes a high aileron downward deflection after the gust subsided, reaching saturation limit. Clearly, this control strategy is not working when rigid body motions are included.

The second control strategy consists of penalizing the first modal velocity instead of the dis-
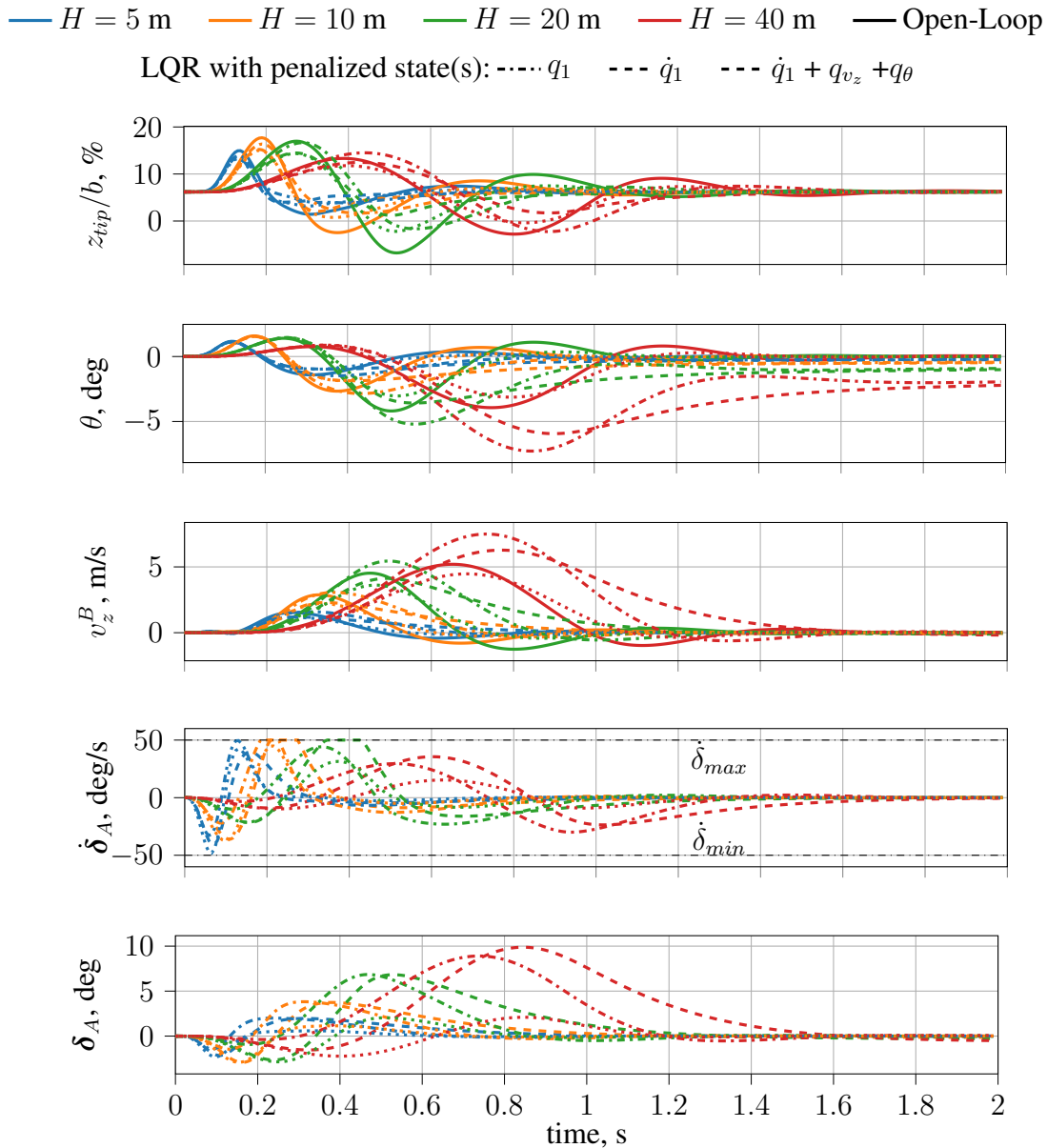
Figure 7: Different LQR penalty strategies for the free-flying SuperFLEXOP the 1-cosine gust with various gust lengths H.

placement. This results in reduced wingtip displacements over all investigated gust lengths here but still causes an unfavourouble enhanced rigid body response. Also the control surface inputs are similarly to the previous control strategy, higher after the gust has subsided, getting even worse for higher gust lengths. It becomes obvious that the elastic/rigid coupling effects become a major consideration in the control strategy. Hence, the last and finalized control strategy is to impose in addition to penalize the modal velocity also the rigid body response by penalizing the modal velocities linked to the rigid body modes of the vertical velocity and pitch. While for the discrete gusts, the same closed-loop response has been found for either penalizing the vertical velocity or pitch, or even both, substantial differences have been found when considering the response of the free-flying SuperFLEXOP to a continuous gust whose rigid body response is shown in Fig. 8.

In the open-loop gust responses, we can observe the SuperFLEXOP repeatedly pitching up and

down while slowing down and speeding up, respectively, in the rigid body pitch θ and horizontal velocity v_x^B. This clearly indicates a present phugoid mode which seems to be unstable. This mode is triggered by various continuous gust inputs but does not show up for discrete gust simulations since the time scales are not large enough. The phugoid mode also becomes apparent in the open-loop nonlinear FOM simulations. We choose to control the thrust of the aircraft, which dampens the phugoid mode, resulting in a longitudinally stable aircraft. When then using this thrust control with the GLA system using sequential loop closing, the chosen penalties for the rigid body motions do make a signficant difference. More precisely, the pitch penalty is important to avoid strong pitch motions induced by the controller. Hence, the pitch related mode penalty (of 1000) has been chosen using the more computational costly continuous gust response. Similarly, the mode corresponding to the vertical rigid body velocity of 0.005 is kept, though it seemingly does not have a big impact on the control response.
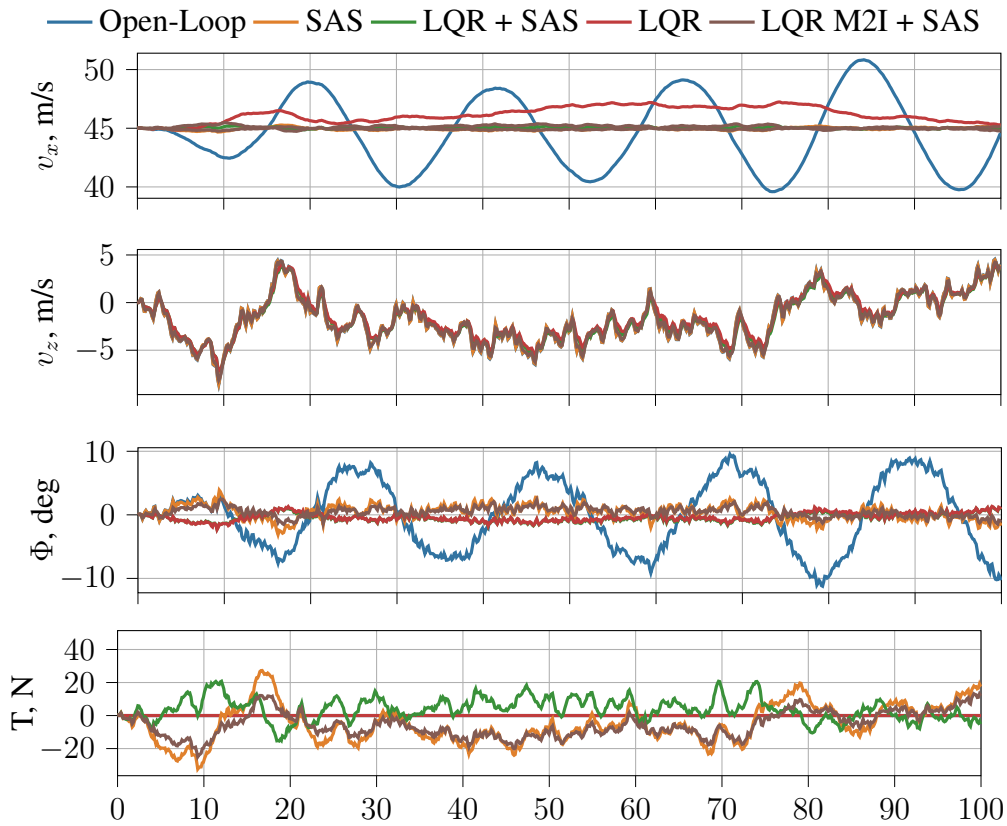
Figure 8: Closed-loop LQR RBM gust response of the linear, free-flying SuperFLEXOP to the continuous gust with $\sigma_w = 2.93$.

The normalized vertical tip displacement z_{tip}/s and control inputs are not visualized in this graph as all of them strongly fluctuate and thus, a statistical description is more valuable and interpretable than a visual one. Fig. 9 shows box-whisker plots for the tip displacement as well as the ailerons deflection and their rate with the box marking the first- and third quartil, and the whisker marking the 99% and 97.5% confidence interval (CI). Because of the present phugoid mode in the open-loop gust response, the results with the SAS system in closed-loop are used as a reference to evaluate the wingtip displacement reduction with the LQR controller in-closed loop. For the SIMO system, we achieve similar wingtip displacement reductions, i.e. about a 9.5% in the RMS value, with and without the SAS system in addition to the LQR controller. Only the mean value is shifted towards smaller wingtip displacements due to the rigid body

response deviating more from the initial conditions. While the aileron deflection rate has a mean close to zero and a symmetric distribution, as expected for the linear gust response, the mean aileron deflection itself is slightly offset. This offset is higher without the SAS system.
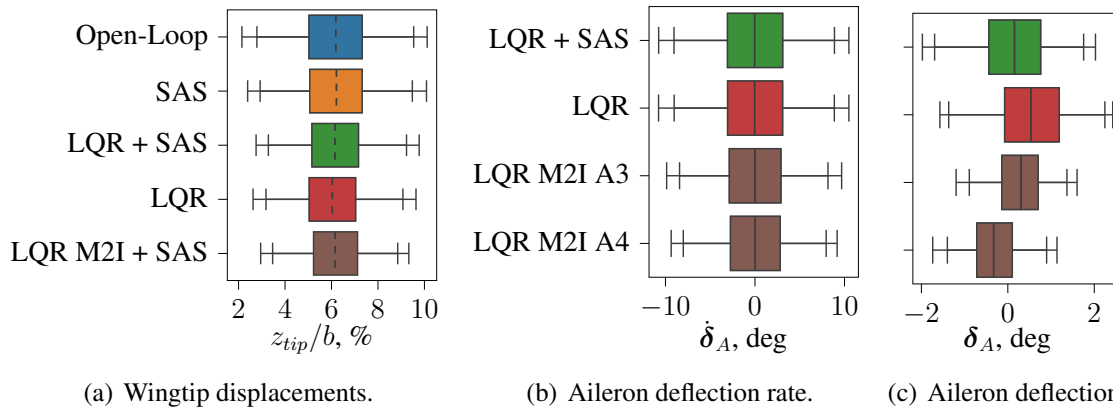

(a) Wingtip displacements.　(b) Aileron deflection rate.　(c) Aileron deflection.

Figure 9: Closed-loop gust response applying the LQG to the linear, free-flying SuperFLEXOP encountering a continuous gust with $\sigma_w = 2.93$.

If we use the two outermost ailerons independently as actuators, we achieve with 16.77% a much higher RMS wingtip displacement reductions than for the SI system for the designed LQR controller. The reason for this becomes apparent when looking at the resulting closed-loop response if actuating all ailerons independently is shown in Fig. 10. Similar to the clamped SuperFLEXOP wing, we had to adjust the penalty, here for the first modal velocity from 0.4 to 1.0. Comparable wingtip displacement reductions are achieved when considering the MI and SI responses. We see slight differences in the rigid body motion response that can be explained by the aileron inputs. More precisely, the inboard aileron deflects downwards instead of upwards and the deflection frequency differs as well. This indicates that the controller uses the inboard aileron not for reducing the first structural modal velocity but rather the rigid body response, especially the pitch mode as seen from the results. We further run the same simulation with only the two outboard ailerons which are again clearly the most effective for GLA. For this choice of actuators, we can almost resemble the SI response, underlining their control effectiveness for wingtip displacement reduction. This control effectiveness can also be observed from the continuous gust responses.

5.2 Kalman Filter Design

Next, we complete the design process for the LQG controller by designing the Kalman filter and selecting appropriate sensors and their combinations. Simpler sensor layouts that have to be proven to be appropriate for load alleviation studies for flexible aircraft are, for example, a combination of an IMU at the centre of gravity of the aircraft to measure local prevailing rigid body motions, and accelerometers at the leading and trailing edges of the wingtip to get an idea of the torsional and bending loads of the wing as done in the GLA wind tunnel tests presented by Ricci et al. [44]. Ting et al [12] have equipped their wind tunnel model with a noncontact Hall-effect sensor to measure the model's pitch angle, unidirectional accelerometers for the structural bending and torsional motion, strain gauges for the out-of-plane bending strain at the wing-root, and rotary potentiometers for the actual control surface deflections. Forte et al [7] analysed the stability margins of their LQG-controller using different configurations of vertical accelerometers and strain gauges. Patartics et al [45] have chosen angular rate measurements of the aircraft pitch and for the wing torsional and bending movement near the wingtip as sensor
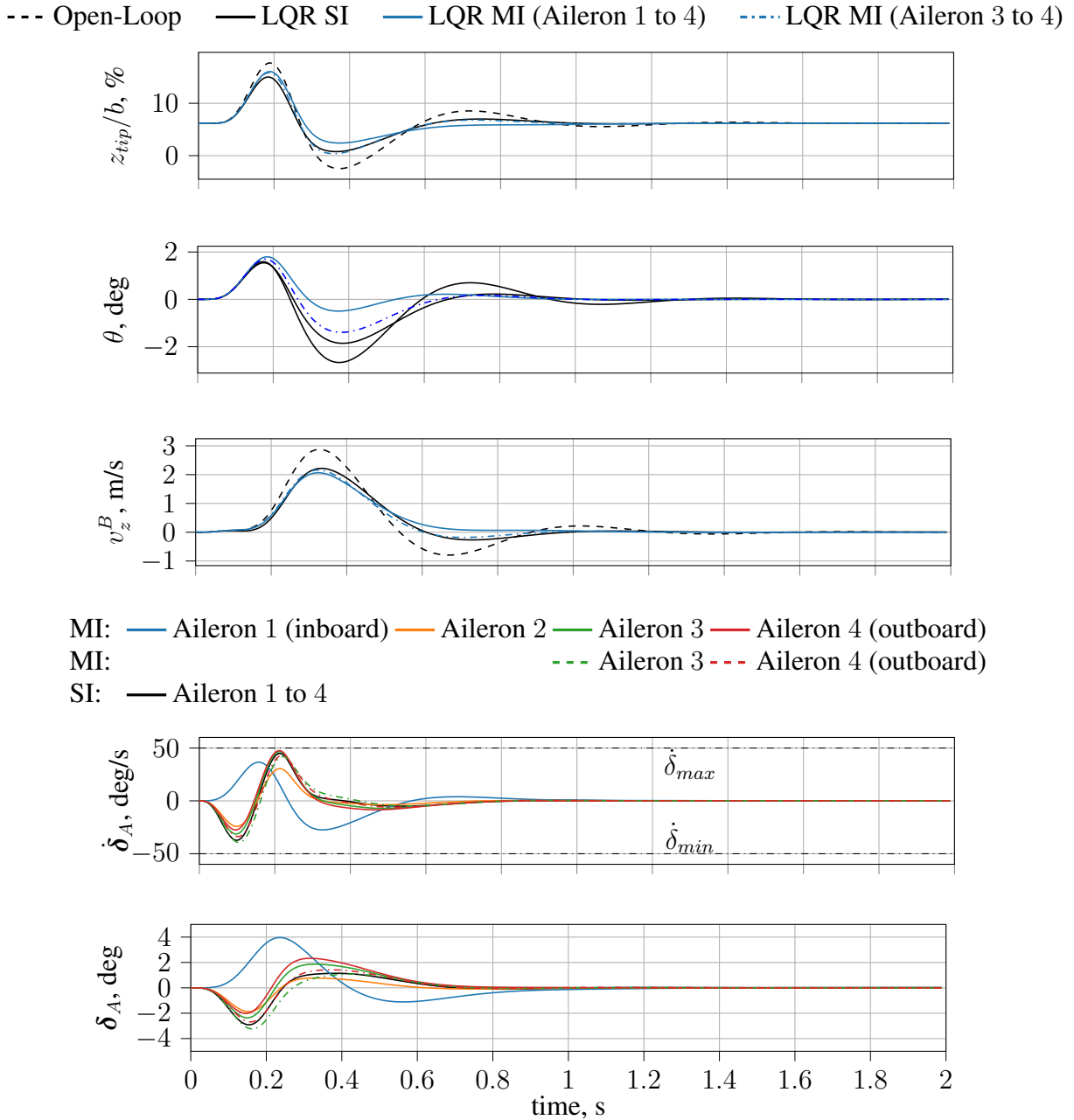
Figure 10: Closed-loop gust response of the linear, free flying SuperFLEXOP to the 1-cosine gust with a gust lengths of $H = 10\,\mathrm{m}$.

readings for an active flutter suppression systems.

These sensor arrangements are easily to implement for the nonlinear and linear aeroelastic systems used in this work. Recalling that the output of our aeroelastic linear system $\boldsymbol{y}_{ae}$ includes the rigid body motions $\boldsymbol{\beta}$, which are similar to the IMU measurements at the center of gravity. Also the accelerometer readings $\ddot{z}$ and angular velocities ω_x and ω_y obtained from gyroscopes can be easily obtained from the structural velocities $\dot{\boldsymbol{\eta}}$ and accelerations $\ddot{\boldsymbol{\eta}}$, respectively. The strain measurements can be estimated from the structural displacement $\boldsymbol{\eta}$.

The Kalman filter performance is assessed with, first, the linear FOM in closed-loop and, second, the nonlinear FOM in open-loop. The open-loop simulation of the nonlinear FOM is

excited by the same gusts as the other systems and a pre-defined aileron deflection input, generated from the linear ROM in closed-loop with the LQR controller. This step is important, especially since our primary goal is to bring the LQG controllers into a closed loop with the nonlinear FOM, which has much more complex dynamics than the linear ROM used to synthesize the LQG controller. By using first the simulations from the open-loop nonlinear FOM, the Kalman Filter design process is computationally more efficient and also serves as evidence of the actuator performance preserved in the linear FOM.

5.2.1 Discrete Gusts

We start with the discrete gust case before considering continuous gusts. With the linear FOM in closed-loop we achieve excellent Kalman Filter performance with all sensor layouts considered. The resulting error between the estimate and actual states between the estimated states of interests, i.e. the penalized first modal displacements and velocities, being of the order of minus four for discrete gusts. This is not surprising as the linear FOM represents well the dynamics of the ROM on which the Kalman Filter is synthesized. We further observed that the Kalman Filter is not sensitive to its tuning parameters, i.e. measurement and process noise covariance matrices which are chosen to be $R = 10^{-6}$ and $Q = 2.3$, respectively.

Next, we evaluate the Kalman Filter performance with the second test case, namely the nonlinear FOM in open-loop. The achieved tip displacement reduction for a gust length of $H = 10\,\mathrm{m}$ and gust intensity of $U_{ds}/U_\infty = 10\,\%$ is comparable for the linear and nonlinear FOM simulations with $25.29\,\%$ and $24.21\,\%$, respectively, for the clamped SuperFLEXOP. For the free-flying SuperFLEXOP, the results are matching even better with $-23.31\,\%$ and $-23.62\,\%$ tip displacement reduction.

The state estimation performance varies substantially as expected. One reason is that due to basic assumptions in the linearized model, the OOP dynamics are very well captured while the IP movements are not. Henceforth, we consider only measurements of the vertical acceleration or the rotations around the chord- and spanwise directions. Another expected reason is due to numerical noise and deviations the linear ROM, the Kalman Filter must be re-tuned to adjust for the different process and measurement noise and is more sensitive to their values.
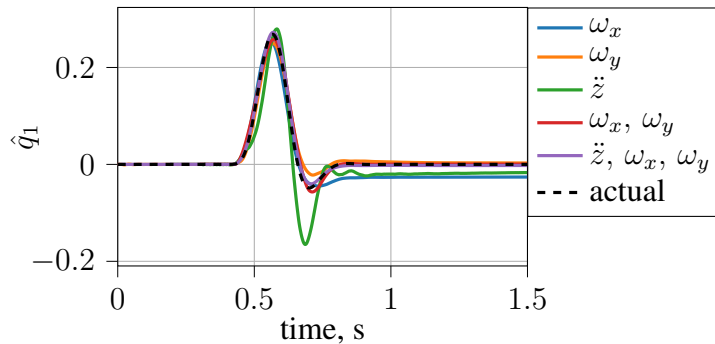

Figure 11: State estimation of first modal displacement q_1 with the nonlinear FOM in open-loop and different sensor layouts.

For the clamped SuperFLEXOP, we achieved a well-performing Kalman Filter performance for $R = 0.1$ for the accelerometers and $R = 10^{-5}$ for the gyroscopes. The resulting state estimation of the modal displacement is shown in Fig. 11. With only accelerometers $\ddot{z}$ used, no tuning could be found for which the modal displacement can be sufficiently observed. Utilizing gyroscopes measuring the velocity ω_x around the spanwise axis, the Kalman Filter observes the peak

modal displacement well but with a small offset at the peak and a steady constant offset after the gust subsides. This steady constant might vanish in the nonlinear FOM in closed-loop simulations. When measuring the velocity around the chordwise axis ω_y, the Kalman Filter observes both extrema with a small offset. When combining both gyroscopes, the offset at the minima vanishes but remains at the peak. The best performance is found with a combination of gyroscopes measuring ω_x and ω_y as well as a vertical accelerometer $\ddot{z}$ with the peak displacement deviating by only $1.5\,\%$.

For the free-flying SuperFLEXOP, values of $R = 100$ for accelerometer and gyroscope sensors performed well. We chose $R = 0.01$ for all rigid body motions except for the rotational velocity around the y^B-axis which is tuned to $R = 10^{-4}$. When including the rigid body motions, interestingly all considered sensor choices result in similiar estimation results with deviations around $-3.8\,\%$ and $-5.5\,\%$ for the minimum and maximum modal velocity peaks, illustrated in Fig. 12. These deviations are within the range of offsets caused by nonlinearities for the examined gust intensities.
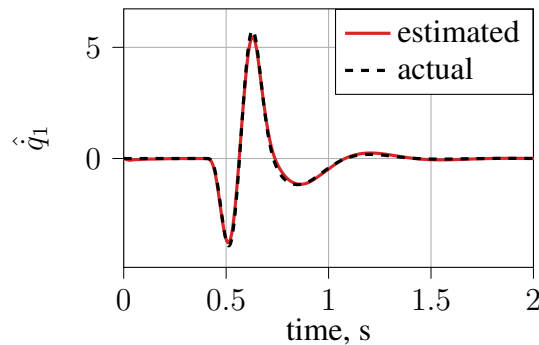

Figure 12: State estimation of the first modal velocity $\dot{q}_1$ with the nonlinear FOM in open-loop.

6 GLA PERFORMANCE TEST WITH NONLINEAR ASE MODEL

We finally apply the GLA controllers in closed-loop simulation with the nonlinear FOM. The nonlinear FOM, operating in SHARPy, therefore communicates with the LQG controller, facilitated in Simulink, via a UDP interface. SHARPy transmits the sensor reading to the controller which in turn computes the control inputs. These control inputs are fed back into the nonlinear aeroelastic FOM simulator as proposed in Fig. 2.

6.1 Clamped SuperFLEXOP

We present next the gust alleviation studies with the nonlinear aeroelastic FOM of the clamped SuperFLEXOP in closed-loop simulations with the LQG controller. We utilize the sensor combination of a vertical accelerometer $\ddot{z}$ and the gyroscopes measuring the angular velocities ω_x and ω_y. The resulting vertical wingtip displacements as well as the controller-generated aileron deflections are shown in Fig. 13 for gust lengths of $H = 5 - 40\,\mathrm{m}$ and an intensity of $U_{ds}/U_\infty = 0.1$. The LQG controller reduces the wingtip displacements for all gust lengths sufficiently. The reductions in tip displacement achieved with the nonlinear FOM in closed-loop are marginally less than those with the linear FOM. These varying levels of reduction are detailed in Table 3, highlighting greater discrepancies in the controller performance for longer gust length $H = 40\,\mathrm{m}$.

This diminished performance in load alleviation could be attributed to a less aggressive control action, evidenced by smaller peak aileron deflection inputs when using the nonlinear FOM in a closed-loop configuration with the LQG controller. This underperformance may stem from the
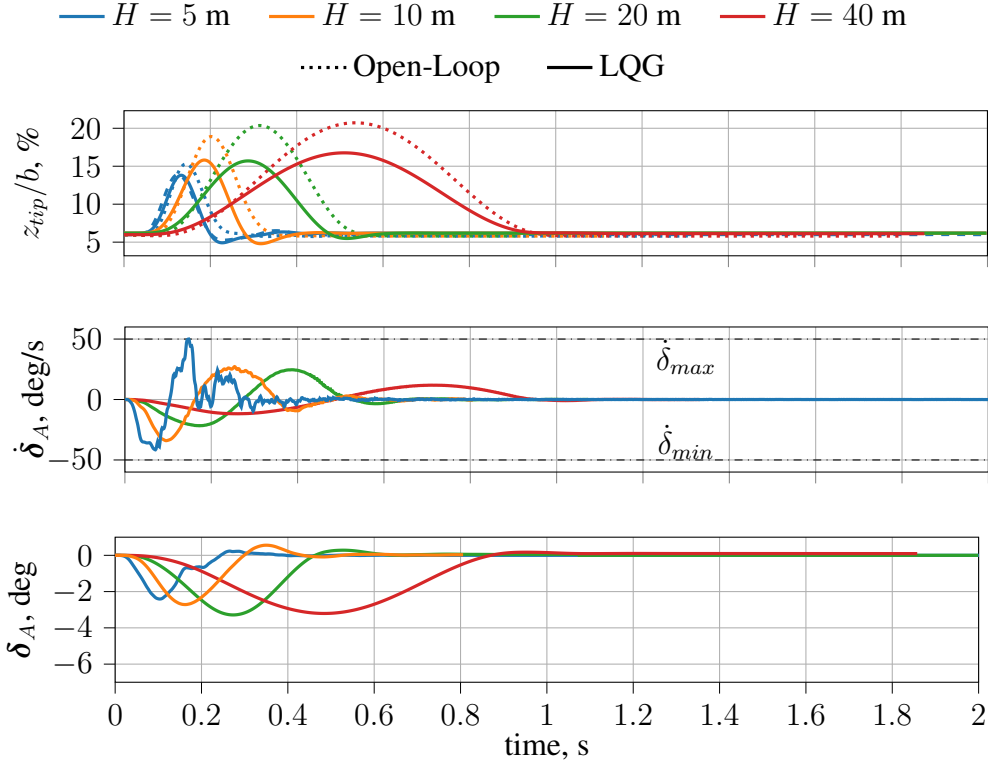
Figure 13: Closed-loop LQG gust response of the nonlinear, clamped SuperFLEXOP to the 1-cosine gust with various gust lengths H.

Table 3: Overview of achieved wingtip reduction for different systems in closed-loop.

System in closed-loop	$H = 5\,\mathrm{m}$	$H = 10\,\mathrm{m}$	$H = 20\,\mathrm{m}$	$H = 40\,\mathrm{m}$
nonlinear	14.9 %	19.5 %	25.3 %	26.9 %
linear	18.9 %	25.3 %	32.5 %	37.1 %

state estimator, whose effectiveness could be compromised by either increased noise levels in the more complex simulations, nonlinearities, or interference effects of the controller with the nonlinear FOM. The deviation in the estimated states compared the states of the linear FOM resulting from the same gust and control input, are $-5.07\,\%$, $-6.06\,\%$, and $-6.44\,\%$, for the gust lengths of $H = 10\,\mathrm{m}$ to $H = 40\,\mathrm{m}$ in increasing order.

The highest error in the state estimation is $9.00\,\%$ for a gust length of of $H = 5\,\mathrm{m}$, for which we observe a high frequency content in the control surface deflection rate. Despite this higher frequency content, the LQG controller is capable of alleviating the loads and stabilizing the wing. From the estimated states, we can conclude a strong excitation of the second OOP bending mode which has neither been captured by the linear FOM in closed-loop nor the nonlinear FOM in open-loop with the pre-defined control input. This indicates an excitation of this mode by the controller.

6.2 Free-Flying SuperFLEXOP

When we include the rigid body motions, the resulting closed-loop gust response for the gust lengths from $H = 5\,\mathrm{m}$ to $H = 40\,\mathrm{m}$ and an intensity of $U_{ds}/U_\infty = 10\,\%$ are displayed in Fig. 14. The closed-loop outcomes, including the wingtip displacements and aircraft pitch, show a reduction across the entire gust interaction when compared to the open-loop response. Although there is still a slight deterioration in the reduction of tip displacements, linked to a less

aggressive control action, relative to the results obtained with the linear FOM in closed-loop, as summarised in Tab. 4. The performance decreases less than in the closed-loop simulations
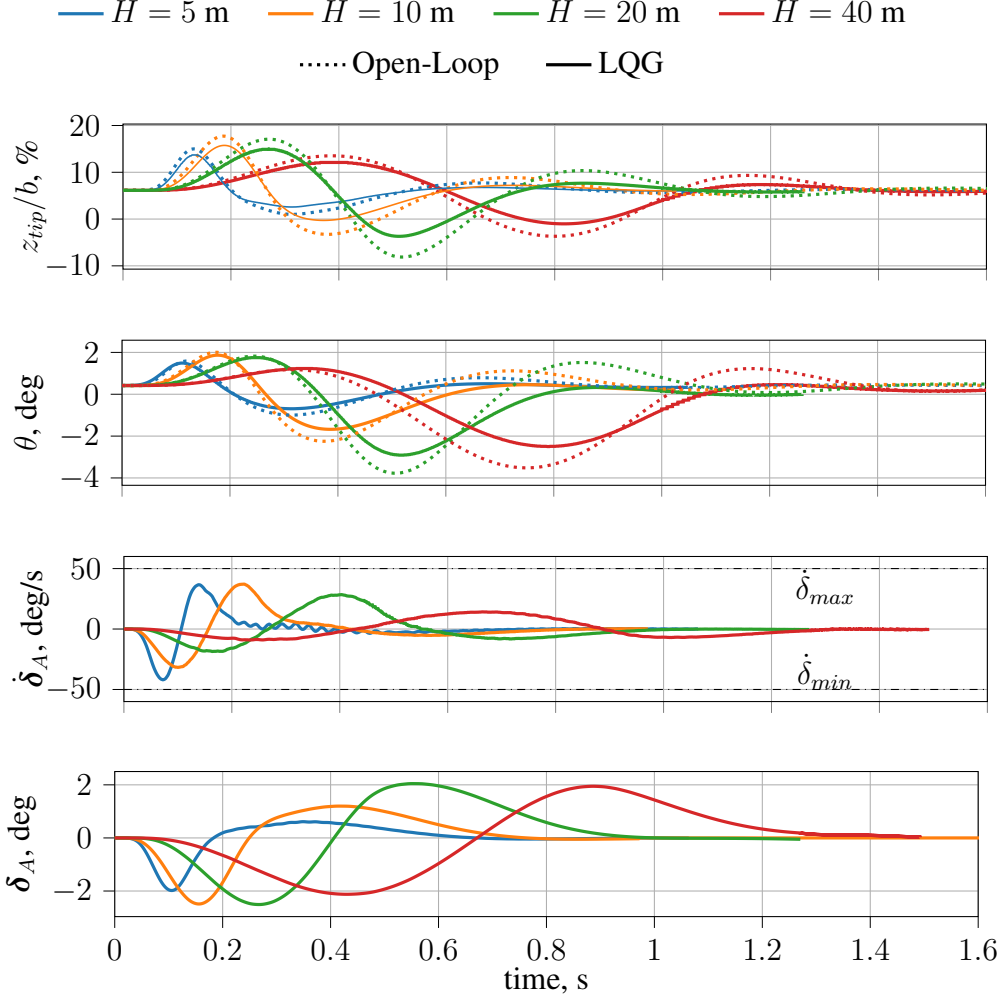

Figure 14: Closed-loop LQG gust response of the linear, free-flying SuperFLEXOP to the 1-cosine gust with various gust lengths H.

of the nonlinear FOM of the clamped SuperFLEXOP. We also see smaller deviations between estimated and linear state of the penalized state, i.e. the first modal velocity $\dot{q}_1$. For $H = 10$ m, this deviation is the highest. Note that due to the different penalized modal states for the clamped and free-flying SuperFLEXOP, the exact errors are not comparable.

Table 4: Overview of achieved wingtip reduction for different systems in closed-loop.

System in closed-loop	$H = 5\,\mathrm{m}$	$H = 10\,\mathrm{m}$	$H = 20\,\mathrm{m}$	$H = 40\,\mathrm{m}$
nonlinear	$14.59\,\%$	$17.48\,\%$	$18.95\,\%$	$19.26\,\%$
linear	$19.46\,\%$	$23.31\,\%$	$24.42\,\%$	$21.611\,\%$

We see the highest error and higher degradation again for the gust lengths corresponding to the highest peak in wingtip displacement, which is here a gust length of $H = 10$ m. To examine the extent of nonlinearities causing this control performance degradation, we simulate the closed-loop gust response of the nonlinear FOM with scaled gust intensities of $U_{ds}/U_\infty = 1\,\%$ and $U_{ds}/U_\infty = 2\,\%$. The resulting reductions in wingtip displacement scale perfectly for these gust intensities as expected for a linear system. When comparing these lower gust intensities with

the initial gust amplitude of $U_{ds}/U_{\infty} = 10\,\%$, the reductions in wingtip displacement scale with an error of $2\,\%$. While this indicates the presence of nonlinearities for high gust intensities, their impact on the control performance is small and, thus, the nonlinearities are not the likely cause of the degradation in control performance. Rather, we suspect it to be caused by a model mismatch of the linear FOM/ROM with the nonlinear FOM. This model mismatch was not apparent in the verification studies of the linearization in open-loop simulations, presented in Ref. [29].

7 CONCLUDING REMARKS

We have developed a control design framework for gust alleviation in highly flexible aircraft, primarily using the nonlinear aeroelastic simulation platform SHARPy. This framework employs SHARPy's nonlinear aeroelastic solver to simulate the SuperFLEXOP model, a flexible representative aircraft. This nonlinear model is linearized around its trim point, creating a linear FOM in state-space form. The linear FOM was then simplified using Krylov-based order reduction techniques on the aerodynamic system, reducing the number of states from over $20,000$ to just $80/122$ for the clamped/free-flying SuperFLEXOP. Using these reduced order models (ROMs), we designed an LQG controller to minimize wingtip displacements induced by discrete and continuous gusts.

Initial tests in linear gust response simulations considering single input systems have showed that the LQR controller effectively reduced wingtip displacement in both configurations. However, incorporating rigid body dynamics necessitated significant adjustments to the LQG controller design due to the strong coupling of structural and rigid body modes. We also have found a present phugoid mode of the aircraft which is excited by continuous gust simulations over a sufficient time scale. This phugoid mode is damped with the thrust controlled by an additional PID controller.

When deploying a multiple input system, using four ailerons individually actuated on each wing, the two outermost ailerons have proved to be the most effective in alleviating the gust-induced wing loads. The LQR controller actuated the inboard aileron to change the rigid body motion which, however, did not result in an improved GLA performance. Subsequently, we have explored various sensor layouts and combinations used for the Kalman Filter and compared the resulting state estimation performance for these sensors. We have found that the Kalman Filter performed better for certain sensor layouts when tested with the nonlinear FOM, while this difference in performance could not be detected with linear FOM.

Ultimately, we have evaluated the LQG controller for the SuperFLEXOP in a simulation that considered nonlinear effects, particularly geometrical ones. While these modifications have achieved similar reductions in vertical wingtip displacement, they resulted in reduced control effectiveness and decreased load alleviation performance which is suspected to be caused by a model mismatch of the linear FOM/ROM with the nonlinear FOM. Further, we have found an excitation of the second OOP bending mode in the closed-loop nonlinear FOM simulations which has not been spotted from the linear FOM closed-loop and nonlinear FOM open-loop results. This has resulted only in higher frequency content in the aileron deflection rate but the controller succeeded in its load alleviation and stabilization objectives. These findings underscore the challenges of modelling complex physics for control.

ACKNOWLEDGEMENT

8 REFERENCES

[1] (ATAG), A. T. A. G. (2021). Waypoint 2050. `https://aviationbenefits.org/media/167417/w2050_v2021_27sept_full.pdf` [retrieved on 6/12/2023].

[2] Kennedy, G., Kenway, G. K., and Martins, J. R. R. A. *High Aspect Ratio Wing Design: Optimal Aerostructural Tradeoffs for the Next Generation of Materials*. doi:10.2514/6.2014-0596.

[3] Palacios, R. and Cesnik, C. E. S. (2023). *Dynamics of Flexible Aircraft: Coupled Flight Mechanics, Aeroelasticity, and Control*. Cambridge Aerospace Series. Cambridge University Press.

[4] Regan, C. D. and Jutte, C. V. (2012). Survey of applications of active control technology for gust alleviation and new challenges for lighter-weight aircraft. Tech. rep., NASA TM-2012-216008.

[5] IATA (2023). Aircraft technology net zero roadmap. `https://www.iata.org/contentassets/8d19e716636a47c184e7221c77563c93/aircraft-technology-net-zero-roadmap.pdf` [retrieved on 4/11/2023].

[6] Burnett, E. L., Beranek, J. A., Holm-Hansen, B. T., et al. (2016). Design and flight test of active flutter suppression on the x-56a multi-utility technology test-bed aircraft. *The Aeronautical Journal*, 120(1228), 893–909. doi:10.1017/aer.2016.41.

[7] Forte, C. J., Nguyen, N. T., and Xiong, J. *Gust Load Alleviation Control and Gust Estimation for a High Aspect Ratio Wing Wind Tunnel Model*. doi:10.2514/6.2023-0881.

[8] Ricci, S., Toffol, F., Marchetti, L., et al. *Design and Experimental Validation of Gust Load Alleviation Systems based on Static Output Feedback*. doi:10.2514/6.2022-0441.

[9] Poussot-Vassal, C., Vuillemin, P., Lepage, A., et al. (2022). Aircraft feedback gust load control design and experimental wing bench validation. *AIAA Scitech 2022 Forum*. doi:10.2514/6.2022-1044.

[10] de Souza, A. d. R., Vuillemin, P., Poussot-Vassal, C., et al. (2023). Gust load alleviation using reduced-order aeroelastic models and observer-based robust control. *Journal of Guidance, Control, and Dynamics*, 46(5), 949–957. doi:10.2514/1.G007153.

[11] Fournier, H., Massioni, P., Pham, M. T., et al. (2022). Robust gust load alleviation at different flight points and mass configurations. *AIAA SCITECH 2022 Forum*. doi:10.2514/6.2022-0285.

[12] Ting, K.-Y., Mesbahi, M., and Livne, E. (2023). Aeroservoelastic wind tunnel evaluation of preview h2 and h gust load alleviation. *Journal of Guidance, Control, and Dynamics*, 46(11), 2044–2062. doi:10.2514/1.G007450.

[13] Artola, M., Goizueta, N., Wynn, A., et al. (2021). Proof of concept for a hardware-in-the-loop nonlinear control framework for very flexible aircraft. In *AIAA Scitech 2021 Forum*. doi:10.2514/6.2021-1392.

[14] de Freitas Virgilio Pereira, M., Kolmanovsky, I. V., Cesnik, C. E., et al. (2021). Time-distributed scenario-based model predictive control approach for flexible aircraft. *AIAA Scitech 2021 Forum*. doi:10.2514/6.2021-0502.

[15] Waite, J., Grauer, J. A., Bartels, R. E., et al. (2021). Aeroservoelastic control law development for the integrated adaptive wing technology maturation wind-tunnel test. *AIAA Scitech 2021 Forum*. doi:10.2514/6.2021-0609.

[16] del Carre, A., Muñoz-Simón, A., Goizueta, N., et al. (2019). SHARPy: A dynamic aeroelastic simulation toolbox for very flexible aircraft and wind turbines. *Journal of Open Source Software*, 4(44), 1885. doi:10.21105/joss.01885.

[17] Géradin, M. and Cardona, A. (2001). *Flexible multibody dynamics: A finite element approach*. Wiley.

[18] Simpson, R. J. and Palacios, R. (2013). Numerical aspects of nonlinear flexible aircraft flight dynamics modeling. In *54th AIAA/ASME/ASCE/AHS/ASC Structures, Structural Dynamics, and Materials Conference*. doi:10.2514/6.2013-1634.

[19] Goizueta Alfaro, N. (2022). *Parametric reduced-order aeroelastic modelling for analysis, dynamic system interpolation and control of flexible aircraft*. Ph.D. thesis, Imperial College London.

[20] Shearer, C. and Cesnik, C. (2006). Modified generalized alpha method for integrating governing equations of very flexible aircraft. *47th AIAA/ASME/ASCE/AHS/ASC Structures, Structural Dynamics, and Materials Conference. Newport, Rhode Island, USA*. doi: 10.2514/6.2006-1747.

[21] Murua, J., Palacios, R., and Graham, J. M. R. (2012). Applications of the unsteady vortex-lattice method in aircraft aeroelasticity and flight dynamics. *Progress in Aerospace Sciences*, 55, 46–72. doi:10.1016/j.paerosci.2012.06.001.

[22] Morino, L. and Bernardini, G. (2001). Singularities in bies for the laplace equation; joukowski trailing-edge conjecture revisited. *Engineering analysis with boundary elements*, 25(9), 805–818. doi:10.1016/S0955-7997(01)00063-7.

[23] Pesmajoglou, S. D. and Graham, J. (2000). Prediction of aerodynamic forces on horizontal axis wind turbines in free yaw and turbulence. *Journal of Wind Engineering and Industrial Aerodynamics*, 86(1), 1–14. doi:10.1016/S0167-6105(99)00125-7.

[24] Maraniello, S. (2016). *Optimal manoeuvres and aeroservoelastic co-design of very flexible wings*. Ph.D. thesis, Imperial College London.

[25] Düssler, S. and Palacios, R. (2024). Enhanced unsteady vortex lattice aerodynamics for nonlinear flexible aircraft dynamic simulation. *AIAA Journal*, 62(3), 1179–1194. doi: 10.2514/1.J063174.

[26] Goizueta, N., Wynn, A., and Palacios, R. (2021). Parametric krylov-based order reduction of aircraft aeroelastic models. *AIAA Scitech 2021 Forum. Online*. doi:10.2514/6. 2021-1798.

[27] Maraniello, S. and Palacios, R. (2019). State-space realizations and internal balancing in potential-flow aerodynamics with arbitrary kinematics. *AIAA Journal*, 57(6), 2308–2321. doi:10.1088/1742-6596/1037/2/022033.

[28] Antoulas, A. C. (2005). *11. Model Reduction Using Krylov Methods*, chap. 11. Society for Industrial and Applied Mathematics, pp. 343–361. doi:10.1137/1.9780898718713.ch11.

[29] Düssler, S., Mylvaganam, T., and Palacios, R. (2024). Modelling for design and performance evaluation of gust load alleviation systems for flexible aircraft. *AIAA SciTech 2024*. doi:10.2514/6.2024-0614.

[30] Brunton, S. L. and Kutz, J. N. (2019). *Data-driven science and engineering: Machine learning, dynamical systems, and control*. Cambridge University Press.

[31] Ogata, K. (1995). *Discrete-time control systems*. Prentice-Hall, Inc.

[32] Grewal, M. S. and Andrews, A. P. (2014). *Kalman filtering: Theory and Practice with MATLAB*. John Wiley & Sons.

[33] Jovanović, M. R., Schmid, P. J., and Nichols, J. W. (2014). Sparsity-promoting dynamic mode decomposition. *Physics of Fluids*, 26(2). doi:10.48550/arXiv.1309.4165.

[34] Welch, G. and Bishop, G. (2001). An introduction to the kalman filter. `https://courses.cs.washington.edu/courses/cse571/03wi/notes/welch-bishop-tutorial.pdf` [retrieved on 4/11/2023].

[35] EASA (2007). *CS-25 Certification Specifications for Large Aeroplane*.

[36] Federal Aviation Administration (1996). *Federal Aviation Regulations Part 25: Airworthiness standards: Transport category airplanes"*.

[37] Fuller, J. R. (1995). Evolution of airplane gust loads design requirements. *Journal of Aircraft*, 32(2), 235–246. doi:10.2514/3.46709.

[38] Sodja, J., Werter, N. P. M., and De Breuker, R. (2021). Aeroelastic demonstrator wing design for maneuver load alleviation under cruise shape constraint. *Journal of Aircraft*, 58(3), 448–466. doi:10.2514/1.C035955.

[39] Stahl, P., Sendner, F.-M., Hermanutz, A., et al. (2017). Mission and aircraft design of flexop unmanned flying demonstrator to test flutter suppression within visual line of sight. In *17th AIAA Aviation Technology, Integration, and Operations Conference*. doi:10.2514/6.2017-3766.

[40] Vanek, B. (2019). D4.10 release of the flight test results and models of the a/c for the community. `https://flexop.eu/static/misc/D410_FLEXOP_y2019m11d30.pdf` [retrieved on 4/11/2023].

[41] Duessler, S., Mylvaganam, T., and Palacios, R. (2023). Lqg-based gust load alleviation systems for very flexible aircraft. *AIAA SciTech 2023 Forum*. doi:10.2514/6.2023-2571.

[42] Pusch, M., Ossmann, D., and Luspay, T. (2019). Structured control design for a highly flexible flutter demonstrator. *Aerospace*, 6(3).

[43] Stanford, B. (2020). Optimal aircraft control surface layouts for maneuver and gust load alleviation. In *AIAA Scitech 2020 Forum*.

[44] Ricci, S., Toffol, F., Marchetti, L., et al. (2022). Design and experimental validation of gust load alleviation systems based on static output feedback. *AIAA Scitech 2022 Forum*. doi:10.2514/6.2022-0441.

[45] Patartics, B., Lipták, G., Luspay, T., et al. (2022). Application of structured robust synthesis for flexible aircraft flutter suppression. *IEEE Transactions on Control Systems Technology*, 30(1), 311–325. doi:10.1109/TCST.2021.3066096.

COPYRIGHT STATEMENT